RESEARCH

Enhanced in vivo blood brain barrier transcytosis of macromolecular cargo using an engineered pH-sensitive mouse transferrin receptor binding nanobody

Thomas J. Esparza[1,2], Shiran Su[1,3], Caroline M. Francescutti[1], Elvira Rodionova[1], Joong Hee Kim[1,2] and David L. Brody[1,4,5*]

Abstract

Background The blood brain barrier limits entry of macromolecular diagnostic and therapeutic cargos. Blood brain barrier transcytosis via receptor mediated transport systems, such as the transferrin receptor, can be used to carry macromolecular cargos with variable efficiency. Transcytosis involves trafficking through acidified intracellular vesicles, but it is not known whether pH-dependent unbinding of transport shuttles can be used to improve blood brain barrier transport efficiency.

Methods A mouse transferrin receptor binding nanobody, NIH-mTfR-M1, was engineered to confer greater unbinding at pH 5.5 vs 7.4 by introducing multiple histidine mutations. The histidine mutant nanobodies were coupled to neurotensin for in vivo functional blood brain barrier transcytosis testing via central neurotensin-mediated hypothermia in wild-type mice. Multi-nanobody constructs including the mutant $M1_{R56H, P96H, Y102H}$ and two copies of the P2X7 receptor-binding 13A7 nanobody were produced to test proof-of-concept macromolecular cargo transport in vivo using quantitatively verified capillary depleted brain lysates and in situ histology.

Results The most effective histidine mutant, $M1_{R56H, P96H, Y102H}$-neurotensin, caused >8 °C hypothermia after 25 nmol/kg intravenous injection. Levels of the heterotrimeric construct $M1_{R56H, P96H, Y102H}$-13A7-13A7 in capillary depleted brain lysates peaked at 1 h and were 60% retained at 8 h. A control construct with no brain targets was only 15% retained at 8 h. Addition of the albumin-binding Nb80 nanobody to make $M1_{R56H, P96H, Y102H}$-13A7-13A7-Nb80 extended blood half-life from 21 min to 2.6 h. At 30–60 min, biotinylated $M1_{R56H, P96H, Y102H}$-13A7-13A7-Nb80 was visualized in capillaries using in situ histochemistry, whereas at 2–16 h it was detected in diffuse hippocampal and cortical cellular structures. Levels of $M1_{R56H, P96H, Y102H}$-13A7-13A7-Nb80 reached more than 3.5 percent injected dose/gram of brain tissue after 30 nmol/kg intravenous injection. However, higher injected concentrations did not result in higher brain levels, compatible with saturation and an apparent substrate inhibitory effect.

Conclusion The pH-sensitive mouse transferrin receptor binding nanobody $M1_{R56H, P96H, Y102H}$ may be a useful tool for rapid and efficient modular transport of diagnostic and therapeutic macromolecular cargos across the blood brain barrier in mouse models. Additional development will be required to determine whether this nanobody-based shuttle system will be useful for imaging and fast-acting therapeutic applications.

*Correspondence:
David L. Brody
david.brody@nih.gov; david.brody@usuhs.edu
Full list of author information is available at the end of the article

Esparza *et al. Fluids and Barriers of the CNS* (2023) 20:64

Page 2 of 17

Background

The efficient delivery of biological macromolecular cargos across the blood brain barrier (BBB) is a major unmet need for diagnostic and therapeutic approaches to brain disorders. In recent years, it has become clear that taking advantage of endogenous receptor mediated transcytosis systems represents a promising approach. To that end, several research groups have developed antibodies and other reagents that bind key targets involved in receptor mediated transcytosis in brain endothelial cells [1, 2]. A common target is the transferrin receptor (TfR) [3, 4], involved in the transcytosis of iron carried by transferrin across the BBB, where it is required for multiple iron-containing proteins in multiple brain cell types [5]. The first clinically approved therapeutic employing a receptor mediated transcytosis BBB shuttle, pabinafusp alfa, consists of a TfR-binding monoclonal antibody fused to the enzyme iduronate-2-sulfatase, which is defective in mucopolysaccharidosis type II (Hunter syndrome) [6, 7]. Additional targets for BBB transcytosis shuttles include the insulin receptor [8, 9], IGF1 receptor [10–12], CD98hc [13, 14], TMEM30 [15], and others [1, 2, 16].

To date, the majority of the candidate BBB transcytosis shuttles have been designed for long-term therapeutic applications, but there remains an unmet need for systems to shuttle biological macromolecular cargos across the BBB optimized for rapid molecular contrast imaging and fast-acting therapeutics. Furthermore, shuttle systems that are readily engineered, inexpensive to produce, simple to handle, and widely accessible to the research community would be a benefit. For specific applications to fast-acting therapeutics and imaging, rapid BBB kinetics would be an advantage. Nanobodies, 12–15 kDa recombinant proteins derived from the binding domains of heavy chain only antibodies from camelids [17, 18], have potential to address this unmet need. Nanobodies are relatively small, readily engineered, and inexpensive to produce. Because of their small size, nanobody systemic kinetics and diffusion within the brain extracellular space may be expected to be relatively fast [19], though they can be engineered to have prolonged half-lives in blood [18]. The first approved nanobody therapeutic, caplacizumab-yhdp which targets von Willebrand factor, has proven to be effective for the rapid treatment of thrombotic thrombocytopenic purpura [20–23]. Additional nanobody-based therapeutics approved for human use include ciltacabtagene autoleucel which targets B-cell

maturation antigen for multiple myeloma [24], envafolimab which targets programmed death ligand 1 for solid tumors [25] and ozoralizumab which targets tumor necrosis factor alpha for rheumatoid arthritis [26]. Other researchers have developed nanobody-based BBB transcytosis reagents that bind to TMEM30 [15], TfR [27, 28], and IGF1R [10, 11].

We previously reported the generation and characterization of a llama nanobody recognizing the extracellular domain of the mouse transferrin receptor called NIH-TfR-M1, referred to as M1 herein. We showed that this nanobody binds independently of the presence or absence of mouse holo-(iron bound) transferrin with relatively high (5 nM) affinity [29]. The M1 nanobody showed modest BBB transcytosis in vivo as measured using a neurotensin (NT)-induced hypothermia assay [29]. Others have reported that antibodies with lower affinities or monovalent binding mediate improved BBB transcytosis [30–32]. It has also been reported that at least some of the intracellular vesicles involved in receptor mediated transcytosis are acidified to approximately pH 5.5 [5], and that pH-dependent binding may favor TfR antibody transcytosis in vitro [33]. Of note, iron dissociates from transferrin under acidic conditions due to protonation of transferrin histidine residues, and apo-transferrin has a much lower affinity for TfR than holo-transferrin [5]. Thus, we reasoned that introduction of histidine residues into M1 could improve BBB transcytosis via accelerated unbinding from TfR at acidic pH while retaining relatively fast binding kinetics at pH 7.4. We were inspired by a previous approach taken using histidine engineering of a TfR-binding single chain variable fragment (scFv) to enhance intracellular accumulation [34], as well as previously reported pH-dependent binding of candidate shuttles to other BBB transport systems [10, 14]. Researchers have introduced histidine mutations for pH-dependent engineering in many other antibodies for other purposes [35–37]. As an initial foray, we previously reported that introduction of a single histidine mutant at residue 96 imparts enhanced unbinding at pH 5.5 and modestly improved in vivo BBB transcytosis as measured using the NT-induced hypothermia assay. However, the $M1_{P96H}$ mutant nanobody was still not effective as a carrier of amyloid-beta binding nanobodies across the BBB in a mouse model of Alzheimer Disease-related amyloid plaque pathology [29]. Therefore, we endeavored to further engineer the M1 nanobody

Esparza *et al. Fluids and Barriers of the CNS* (2023) 20:64

Page 3 of 17

for more extensive pH-dependent unbinding while retaining high affinity at pH 7.4. To this end, we produced 39 additional histidine mutant versions of M1, and characterized them both in vitro and in vivo. One version with 3 histidine mutations, $M1_{R56H, P96H, Y102H}$, demonstrated nearly threefold greater unbinding at pH 5.5 compared with pH 7.4 in vitro, greater than 24-fold stronger NT-induced hypothermia effects than $M1_{P96H}$, and capacity to transport more than 3.5% of the injected dose of a proof-of-concept biological macromolecule cargo per gram of brain across the BBB in vivo at 4 h after intravenous injection. This triple histidine mutant TfR-binding nanobody may have potential as a BBB transcytosis shuttle for fast-acting therapeutics and molecular contrast imaging applications.

Methods

Development of mouse transferrin receptor binding nanobodies

The production and development of the lead candidate nanobody NIH-TfR-M1 was described previously [29]. Briefly, an adult llama was immunized with a recombinant protein consisting of the extracellular domain of the mouse transferrin receptor. Post-immune B cell lymphocyte DNA was used to generate a phage display library. Panning the phage display library using immobilized recombinant mouse transferrin receptor extracellular domain yielded several candidate nanobodies including M1, 4E6 and 1E5. Characterization of 4E6 and 1E5 will be reported separately.

Expression in *E. coli* and purification

Expression of 6xHis tagged nanobodies in *E. coli* was described previously [29]. Briefly, nanobody constructs under the control of the lacZ promotor and an N-terminal pelB periplasmic translocation sequence were cloned into the pHEN2 phagemid vector and transformed into TG-1 competent *E. coli*. Sequence-confirmed clones were grown to mid-logarithmic phase (optical density = 0.6) and expression was induced by addition of 1 mM isopropyl-β-d thiogalactoside (IPTG) followed by overnight expression at 30 °C and 250 rpm. The periplasmic compartment was gently released by osmotic shock and the nanobody construct purified using HisPur™ Ni–NTA resin. Endotoxin was removed using High-Capacity Endotoxin Removal Resin (Pierce) and confirmed to be < 0.5 endotoxin units/mg of total protein. The constructs were polished with size exclusion chromatography (SEC) using a Superdex™75 GL 10/300 column, injected in a maximum volume of 1-mL and eluted at 1 mL/min at room temperature into a 96-well collection block for fractionation. Typical final yield was 1 to 10 mg/100 mL culture of purified nanobody.

Transferrin receptor ELISA with pH-dependent wash steps

Plate-based measurements of nanobody construct affinities were performed as described previously [29]. Briefly, 96-well plates were coated with 2 µg/mL recombinant mouse transferrin receptor extracellular domain (amino acids 89–763) overnight at 4 °C, followed by blocking with 1% (w/v) bovine serum albumin (BSA) in 1×Phosphate-Buffered Saline (PBS) for 1 h and incubated for 1 h at room temperature with varying concentration of nanobody constructs. To assess pH-dependent unbinding, three washes were performed at either pH 7.4 or pH 5.5 for 10 min each. Then bound nanobody constructs were detected with peroxidase conjugated goat anti-alpaca VHH domain specific antibody (#128–035-232, Jackson Immuno Research) followed by colorimetric development with tetramethylbenzidine measured at 650 nm absorbance on a Biotek plate reader.

Site-directed mutagenesis

Site-directed mutagenesis was performed as described previously [29]. Briefly, single histidine point mutations were generated using the Q5 Site-Directed Mutagenesis kit (New England Biolabs) with DNA oligonucleotides incorporating the mutation. The introduction of the point mutation was confirmed by Sanger sequencing before proceeding to protein expression and purification. For instances of multiple histidine point mutations, the entire nanobody fragment was synthesized (Twist Bioscience) and cloned into the pHEN2 phagemid for expression and purification as described above.

Mice

All animal studies were performed in accordance with guidelines established by the National Institutes of Health for the care and use of laboratory animals (NIH publication 85–23, revised 2011) and approved by the National Institute of Neurological Disorders and Stroke (NINDS)/ National Institute on Deafness and Other Communication Disorders (NIDCD) Animal Care and Use Committee in the National Institutes of Health (NIH) Clinical Center (Protocol Number: 1406–21). Adult male and female C57BL/6J mice were obtained from Jackson labs (stock# 000664) at 8 weeks of age. They were housed in at 4–5 mice per cage for at least 1 week before starting experiments. For terminal experiments, mice were deeply anesthetized with 5% isoflurane mixed with medical air and euthanized by transcardiac perfusion with ice cold heparinized saline.

NT construct fabrication

Nanobody constructs including the NT peptide were constructed as previously described [29]. Briefly, DNA

Esparza *et al. Fluids and Barriers of the CNS*   (2023) 20:64

Page 4 of 17

constructs including nanobodies, (Gly-Gly-Gly-Ser)$_3$ linkers, and the 13 amino acids encoding the NT peptide (ELYENKPRRPYIL) were cloned in-frame, expressed by IPTG induction, and purified as described above. Typical final yield was 1 to 10 mg/100 mL culture of purified nanobody.

In vivo assessment of NT-induced hypothermia

Assessments of NT-induced hypothermia were performed as described [29]. Briefly, adult male and female C57BL/6J mice were weighed, abdominal fur was removed, and tails were warmed with a heating pad while mice were under isoflurane anesthesia. Investigators blinded to the identity of the injected constructs randomly assigned mice to injection with one of several constructs or controls between 0600 and 1200. Each construct was tested in at least 3 mice. Temperature measurements were obtained using an infrared thermometer applied to the abdomen while the mice were placed briefly under isoflurane anesthesia. Baseline temperatures were recorded serially prior to injection to ensure stability. Tail veins were injected with approximately 10 µl per gram body weight of nanobody constructs using a 30 gauge needle in PBS at pH 7.4. Temperature measurements were obtained every 20–30 min for up to 180 min. Mice were allowed to recover from anesthesia between temperature measurements and observed for adverse effects. Individual mice were used for up to 3 experiments separated by at least 7 days. We have observed that after 3 experiments, hypothermia responses became inconsistent, even when using previously well-characterized NT constructs. Therefore, individual mice were not used for more than 3 experiments.

Multi-nanobody construct fabrication and characterization

Construct fabrication was performed as described previously [29]. DNA sequences for the 13A7 nanobody and the Nb80 nanobody were generated based on *E. coli* preferred codon usage. Nanobody constructs included (Gly-Gly-Gly-Ser)$_3$ linkers. Size and purity were assessed using size exclusion chromatography and SDS PAGE. No major aggregation or degradation products were observed using size exclusion chromatography. SDS PAGE band densities were analyzed using ImageJ.

Nanobody biotinylation

The incorporation of biotin moieties for downstream detection of nanobody constructs was achieved using a fivefold molar excess of EZ-link-NHS-PEG4-biotin (#21330, Thermo Fisher) with nanobody constructs in 50 mM sodium carbonate buffer, pH 8.5 for 1 h at room temperature. The unreacted biotin reagent was removed using a 5-mL desalting column on an AKTA Pure FPLC system.

Blood and brain tissue sampling

Following tail-vein injection of nanobody constructs, mice were placed under 5% isoflurane anesthesia at the specified terminal time points. Under maintained anesthesia, the right atrium was cut and approximately 100 µl of whole blood collected into heparinized tubes. Subsequently, a 23-gauge needle was used to perfuse with heparinized ice-cold normal saline through the left ventricle. Following complete perfusion, the whole brain was extracted and bisected into separate hemispheres. The left hemisphere was placed into 4% (w/v) paraformaldehyde overnight at 4 °C. The right hemisphere was snap frozen on dry ice prior to storage at −80 °C for downstream capillary depleted homogenate preparation. Following 24-h fixation of the left brain hemisphere, fixative was replaced with 30% sucrose and allowed to equilibrate at 4 °C for 48-h prior to sectioning the tissue using a freezing sliding microtome producing 50µm thick sections stored in 1xPBS containing 0.05% sodium azide prior to histological assessment.

Capillary depletion of brain lysates

The parenchymal fraction was physically separated from the associated vessel components using a modification of previously published methods [38]. Briefly, brain hemispheres were weighed and then dounce homogenized in 1 mL ice-cold HEPES-buffered saline (HBSS) with a fixed number of dounces within sample set to reduce variability. The homogenate was transferred to a 1.5 mL microcentrifuge tube and spun at 2000×*g* for 10 min at 4 °C. The parenchymal fraction supernatant was transferred to a new tube, snap frozen on dry ice and stored at −80 °C until assessed for nanobody concentration by ELISA. The vessel containing pellet was resuspended in 1 mL of HBSS containing 18% (w/v) dextran (molecular weight 60–70 kDa) using a wide-bore pipet, and then spun at 4400×*g* for 15 min at 4 °C. The myelin layer was carefully removed using a disposable cotton applicator and a wide-bore pipet. Then the underlying vessel-enriched pellet was resuspended in HBSS containing 1% (w/v) BSA. The solution was transferred to a 40µm cell strainer, and the vessels were washed twice with HBSS containing 1% (w/v) BSA, followed by transfer of the vessels into a new microcentrifuge tube using a wide-bore pipet. The vessels were spun at 2000×*g* for 5 min at 4 °C, and the supernatant was removed to deplete the BSA content. The pellet was then resuspended in 1 mL HBSS and spun down again at 2000×*g* for 5 min at 4 °C. The supernatant was carefully removed, and the pellet was then snap frozen on dry ice and stored at −80 °C.

In situ histochemistry

The presence of biotinylated nanobody construct in situ was performed using streptavidin-peroxidase detection followed by an amplification step as follows: Gentle antigen retrieval was performed by incubation at 60 °C in 50 mM sodium citrate buffer, pH 6.0 for 10 min. Endogenous peroxidase was then quenched by incubation in 3% (v/v) hydrogen peroxide for 10 min. The tissue was then blocked with 5% (v/w) BSA in 1xPBS containing 0.05% Tween-80 for 1 h at room temperature. An initial avidin-peroxidase step was performed using Vectastain Elite ABC-HRP (#PK-6100, Vector Laboratories) reagent diluted 1:400 in 1xPBS (complexed 20 min before use) for 1 h at room temperature. The biotin signal was then amplified by addition of a 2 μM solution of tyramide-biotin reagent (#92176, Biotium) in 10 mM Tris, pH 7.5 containing 0.0015% (v/v) hydrogen peroxide for 10 min at room temperature. A final avidin-peroxidase step was performed for 1 h at room temperature. Chromogenic development was performed using diaminobenzidine. The same development termination time was used for all tissues in a sample set to provide for comparative assessments. Tissue was washed three times for 5 min each in 1xPBS between each of the above steps.

Ex vivo immunohistochemistry

Detection of ex vivo nanobody construct immunoreactivity in 50 μm thick coronal brain sections was performed as follows: Gentle antigen retrieval was performed by incubation at 60 °C in 50 mM sodium citrate buffer, pH 6.0 for 10 min. Endogenous peroxidase was then quenched by incubation in 3% (v/v) hydrogen peroxide for 10 min. The tissue was then blocked with 5% (v/w) BSA in 1xPBS containing 0.05% Tween-80 for 1-h at room temperature. Biotinylated nanobody construct was diluted to 50 nM in 0.5% (w/v) BSA in 1xPBS and tissue incubated overnight at 4 °C. Avidin-peroxidase detection was performed using Vectastain Elite ABC-HRP, prepared as described above, for 1 h at room temperature. Chromogenic development was performed using diaminobenzidine, the same development termination time was used for all tissues in a sample set to provide for comparative assessments. Tissue was washed three times for 5 min each in 1xPBS between each of the above steps.

Percent injected dose per gram of brain calculation

Calculations were performed using the following formula:

$$\frac{\%ID}{gram_{brain}} = \frac{\frac{measured\ construct\ in\ brain\ sample(nmol)}{injected\ construct(nmol)} * 100}{brain\ sample\ mass(g)}$$

where

$$\begin{aligned}&measured\ construct\ in\ brain\ sample(nmol)\\&= measured\ brain\ concentration(nM)\\&\quad * brain\ lysate\ volume(L)\end{aligned}$$

and

$$\begin{aligned}&injected\ construct\ (nmol)\\&= injected\ dose\left(\frac{nmol}{kg}\right)\\&\quad * mouse\ body\ weight\ (kg)\end{aligned}$$

Statistical analyses

Statistical analyses were performed using GraphPad Prism 9.5.0. Affinity measurements were calculated using the "Dose Response" function in the "Nonlinear Regression" analysis group. Simple two way ANOVAs rather than repeated measures ANOVAs were performed because data at each time point was taken from different groups of animals. Statistical significance was defined as 2-sided p-values < 0.05 after correction for multiple comparisons. Sidak's multiple comparisons test was performed for post-hoc pairwise comparisons.

Model fitting

GraphPad Prism 9.5.0 was used for model fitting. The models used were "Specific binding with Hill slope" and "Substrate inhibition" in the "Nonlinear Regression" analysis group. Both models had 3 free parameters and were fit to 22 pairs of injected dose vs. brain lysate concentration data points, leaving 19 degrees of freedom. Fit parameters were obtained using least squares.

Results

Engineering the M1 mouse TfR binding nanobody with histidine mutations for pH-dependent binding

Our goal was to engineer a mTfR-binding nanobody for use as a BBB transcytosis shuttle. We refined our previously reported lead candidate llama nanobody recognizing the extracellular domain of the mouse TfR called M1 by introducing a series of histidine mutations and assessing their effects on pH dependent binding in vitro. We used a plate-based assay to assess relative unbinding at pH 5.5 vs. pH 7.4. In this assay, several concentrations of each M1 variant were bound to 96 well plates coated with mTfR at pH 7.4 and room temperature. Relative apparent mTfR unbinding was assessed by measuring the nanobody remaining after three 10 min washes at either pH 7.4 or pH 5.5 (Fig. 1). Unbinding of the original M1
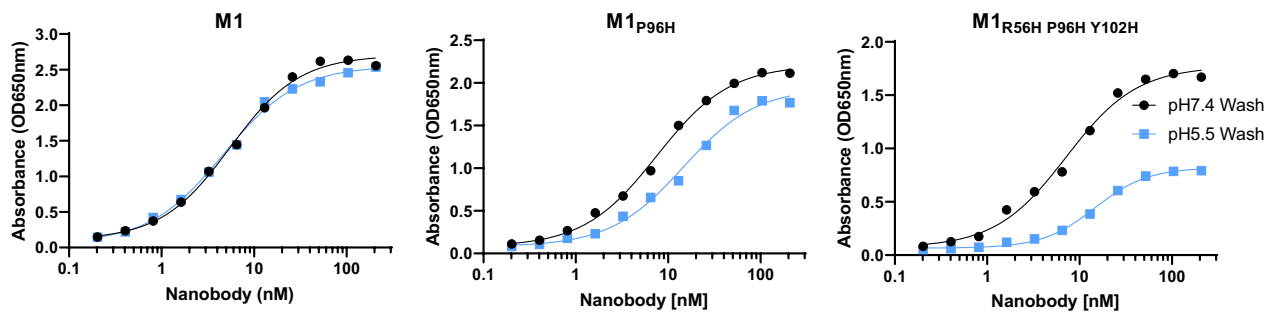
Fig. 1 Binding and pH-dependent unbinding of M1 nanobody and histidine mutants to recombinant mTfR apical domain. Each nanobody was bound at multiple concentrations to 96 well ELISA plates coated with recombinant mTfR at pH 7.4, then washed at either pH 7.4 or pH 5.5. The original M1 has very little pH dependent unbinding, whereas the $M1_{P96H}$ mutant had an average of 1.46-fold more unbinding at pH 5.5 and the $M1_{R56H, P96H, Y102H}$ mutant had an average of 2.63-fold more unbinding at pH 5.5

was similar after three 10 min room temperature washes at pH 7.4 vs. pH 5.5, indicating a lack of pH dependence. In contrast, several of the M1 histidine mutant had > two-fold greater unbinding at pH 5.5 vs. pH 7.4. We did not observe any histidine mutants with the reverse effect: greater unbinding at pH 7.4 than at pH 5.5. Several histidine mutants imparted greater unbinding at pH 5.5 vs. pH 7.4 but had reduced overall affinity. Other histidine mutants did not impart pH-dependent unbinding. The mutants, their affinities at pH 7.4, and their relative unbinding at pH 5.5 vs pH 7.4 are shown in Table 1. The effects of multiple histidine mutants were not necessarily additive; double, triple, quadruple, and quintuple mutants did not necessarily have greater pH-dependent unbinding than otherwise similar mutants with smaller numbers of histidines. One mutant retained high affinity and imparted steeply pH-dependent unbinding. Specifically, $M1_{R56H, P96H, Y102H}$ had 2.63-fold greater unbinding at pH 5.5 vs pH 7.4 while retaining affinity < 10 nM at pH 7.4. Exemplar binding curves for the original M1, the previously reported $M1_{P96H}$ and the triple histidine mutant $M1_{R56H, P96H, Y102H}$ are shown in Fig. 1. Thus, histidine mutations introduced a range of enhanced unbinding rates at pH 5.5 in vitro, and one triple histidine mutant imparted both enhanced pH-dependent unbinding with preserved high affinity at pH 7.4.

In vivo BBB transcytosis assessed via neurotensin-induced hypothermia

We next asked whether these histidine mutants conferred greater BBB transcytosis in vivo using NT-induced hypothermia assays. This assay has previously been used to efficiently screen candidate BBB crossing shuttle systems [10, 27–29, 39–41]. After intravenous injection of 25 nmol/kg of $M1_{R56H, P96H, Y102H}$-NT fusion, mouse temperatures dropped profoundly by up to 8 °C (Fig. 2). Other histidine mutants with a range of affinities also had

substantially more potent effects than the original M1 or $M1_{P96H}$ with temperature drops of 2–6 °C after intravenous injection of 25 nmol/kg (Table 1). In contrast, M1 and $M1_{P96H}$ required higher doses to produce detectable drops in body temperature (Fig. 2). An M1 variant with alanine mutations at residues 100b and 100c in the Kabat numbering scheme ($M1_{AA}$) which did not bind TfR also did not cause detectible hypothermia at doses as high as 600 nmol/kg (Fig. 2). M1 mutants with very low affinity generally did not produce substantial hypothermia, nor did mutants with relatively modest pH-dependent binding (Table 1, Additional file 1: Fig. S1). As noted, the NT-induced hypothermia assays were performed in a randomized, blinded fashion. These results indicated that M1 histidine mutants with pH-dependent unbinding could produce potent NT-induced hypothermia, consistent with the hypothesis that they shuttle NT across the BBB more efficiently in vivo.

Rapid shuttling of macromolecular cargoes across the BBB in vivo

As noted above, NT-induced hypothermia can be considered an efficient screening assay. However, it is not a definitive test of generalized BBB transcytosis. Therefore, we used two additional methods to assess the capacity of $M1_{R56H, P96H, Y102H}$ to shuttle macromolecular cargoes across the BBB in vivo: capillary-depleted brain homogenates and in situ histochemistry. For proof-of-concept assessments, we created a three nanobody construct: $M1_{R56H, P96H, Y102H}$ plus two tandem copies of the P2X7 receptor binding nanobody 13A7 [42] produced as a single protein using glycine-serine linkers between nanobodies (Fig. 3A). As a non-binding control, we created a construct with $M1_{R56H, P96H, Y102H}$ and two tandem copies of the human amyloid-beta receptor binding nanobody Nb3 [29, 43] (Fig. 3B). Nb3 has no known targets in the wild-type mouse brain. The three nanobody constructs

Table 1 Mouse TfR binding nanobody histidine mutants tested in vitro and in vivo

Nanobody	mTfR affinity pH 7.4 (nM)	Apparent mTfR unbinding ratio at pH 5.5 vs pH 7.4	NT-mediated Hypothermia (°C)
M1	5.11	1.01	0
M1: P96H	7.031	1.46	1
M1: Y98H	2509	1.28	2.5
M1: S99H	> 5000	1.01	1
M1: T100aH	55.31	1.05	1.5
M1: T100bH	30.12	1.24	0
M1: R100dH	1294	1.01	0
M1: L100eH	203	1.32	0
M1: D100fH	> 5000	1.58	0
M1: S100gH	> 5000	1.03	0
M1: K100iH	> 5000	1.42	0
M1: D101H	25	1.32	1.5
M1: Y32H, P96H	373	2.57	0
M1: G65H, P96H	> 5000	2.09	1
M1: P96H, Y98H	33.18	2.48	1.2
M1: P96H, S100H	1140	1.02	0
M1: P96H, D101H	242	2.65	7.5
M1: P96H, Y102H	11.65	2.33	6
M1: Y98H, Y102H	> 5000	1.29	5
M1: D31H P96H Y102H	95	1.13	0
M1: R33H P96H Y102H	1545	1.10	0
M1: R56H, P96H, Y98H	> 5000	0.98	1.5
M1: R56H, P96H, D101H	> 5000	1.78	0
M1: R56H, P96H, Y102H	6.653	2.63	8
M1: R56H, Y98H, D101H	52.6	1.04	0
M1: R56H, Y98H, Y102H	> 5000	0.99	0
M1: R56A, P96H, Y102H	1.7	2.59	0
M1: Y59H, P96H, Y102H	888	2.07	1
M1: A60H, P96H, Y102H	> 5000	ND	0
M1: P61H, P96H, Y102H	148	2.13	1
M1: S62H, P96H, Y102H	> 5000	2.18	1.5
M1: A64H, P96H, Y102H	> 5000	1.79	0
M1: S70H, P96H, Y102H	78	1.64	0
M1: P96H S99H D101H	301	2.43	2
M1: P96H S99H Y102H	> 5000	2.52	2.5
M1: P96H, D101H, Y102H	> 5000	2.42	0
M1: C22A C92A P96H D101H	35.76	1.03	0
M1: C22A C92A P96H Y102H	17.56	1.07	0
M1: R56H, P96H, Y98H, Y102H	> 5000	1.00	0
M1: R56H, P96H, S99H, Y102H	246	2.04	5.5
M1: Y32H, R56H, P96H, S99H, Y102H	> 5000	1.11	0

In vitro assessments included a) ELISA-based affinity measurements vs. recombinant mTfR extracellular domain conducted at pH 7.4 at room temperature, and b) plate-based unbinding assays conducted by binding nanobodies to recombinant mTfR extracellular domain at pH 7.4, then washing at either pH 5.5 or pH 7.4 at room temperature. In vivo assessments consisted of blinded measurements of mouse peak hypothermia following iv injection of 25 nmol/kg of each of the nanobodies fused with neurotensin (NT) (n = 3–6 mice per construct). ND: not determined due to low binding

Esparza *et al. Fluids and Barriers of the CNS*   (2023) 20:64

Page 8 of 17
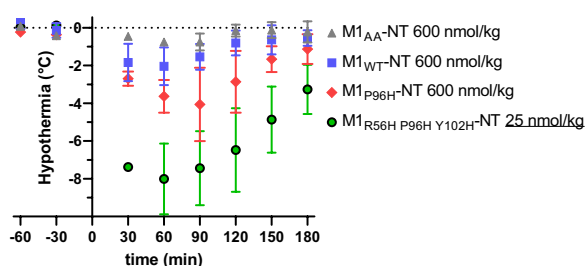
Fig. 2 M1 mTfR binding nanobody–NT fusions for assessment of central nervous system target engagement. Blinded assessment of M1 variants injected iv into wild-type mice (n = 3/group). M1 and M1$_{P96H}$ mutant caused modest hypothermia at 600 nmol/kg. M1$_{AA}$ (non TfR binding) TfR caused no detectible hypothermia. M1$_{R56H, P96H, Y102H}$ caused pronounced hypothermia at 25 nmol/kg

were produced at final levels of 1 – 10 mg per 100 mL of culture media in *E. coli.* The constructs were > 70% pure based on quantification of SDS PAGE band densities (Additional file 1: Fig. S2A). We biotinylated the three nanobody constructs at random lysines to facilitate detection. Biotinylation at 5:1 stoichiometry yielded an average of 1.05 ± 0.1 to 1.5 ± 0.06 biotin adducts per nanobody, indicating relatively sparse labeling given that there are 4–5 lysines per nanobody.

There was clear evidence of BBB transcytosis of the M1$_{R56H, P96H, Y102H}$ 13A7-13A7 construct after intravenous injection in mice. The biotinylated three nanobody construct was readily detected in capillary-depleted brain homogenates after iv injection of 30 nmol/kg. Capillary-depleted lysate levels rose from 30 min to 1 h, peaked at 1 h, and remained approximately 60% of peak at 8 h (Fig. 3C). Levels of the control BBB crossing three nanobody construct in which 13A7 was replaced by Nb3 followed different kinetics, with similar levels at 30 min but < 15% retained at 8 h (Fig. 3D). At 8 h, the brain levels of M1$_{R56H, P96H, Y102H}$ 13A7-13A7 were ~ sevenfold higher than M1$_{R56H, P96H, Y102H}$-Nb3-Nb3 (1.39 vs. 0.2 nM). Two way ANOVA was used to analyze the capillary depleted brain homogenate data. There were significant main effects of both construct (M1$_{R56H, P96H, Y102H}$-13A7-13A7 vs. M1$_{R56H, P96H, Y102H}$-Nb3-Nb3; $F_{1,20}$ = 151, p < 0.0001) and time ($F_{4,20}$ = 9.9, p = 0.0001), as a well as a significant construct x time interaction ($F_{4,20}$ = 9.7, p = 0.0002). Post-hoc comparisons were significant for all time points except 30 min (p < 0.0001). Capillary depletion was approximately 98–99% effective, based on Claudin 5 ELISA measurements in crude vs capillary depleted lysates (Additional file 1: Fig. S3A). Western blots for VE cadherin confirmed capillary depletion (Additional file 1: Fig. S3B). Biotinylated nanobody construct levels in the capillary fractions were elevated at 30 min and 1 h but below the limit of reliable quantitation (< 0.166 to

0.2 nM) at later times (Additional file 1: Fig. S4A-B). The time course of the constructs in blood showed a mono-exponential decline with half-lives of approximately 21 and 11 min respectively (Fig. 3E, F). These capillary depleted lysate results were compatible with the hypothesis that M1$_{R56H, P96H, Y102H}$ was capable of shuttling proof-of-concept biological macromolecules across the BBB in vivo and that brain kinetics depended on brain target engagement.

Prolonged blood half-life increases peak brain levels
In order to determine whether higher brain concentrations of nanobody constructs could be obtained by prolonging blood half-life, we added an albumin binding nanobody called Nb80 [44] making a four nanobody construct (Fig. 4A). TfR binding, P2X7 receptor binding, and albumin binding functions were retained in the biotinylated four nanobody constructs, with characteristics comparable to those of the individual nanobodies. A control four nanobody construct in which 13A7 was replaced with Nb3 was also produced. The four nanobody constructs were produced at final levels of 1–10 mg per 100 mL of culture media in *E. coli.* Again, the constructs were > 70% pure as assessed by SDS PAGE (Additional file 1: Fig. S2B). The time course of the four nanobody construct in blood showed a mono-exponential decline with half-life of approximately 2.6 h (Fig. 4B).

Again, BBB transcytosis of the four nanobody construct was clearly observed in capillary-depleted brain homogenates, with peak levels occurring later than for the three nanobody construct. Capillary-depleted lysate levels rose from 30 min to 4 h, peaked at 4–8 h at levels approximately 50% higher than the peak concentration attained by the three nanobody construct, and were > 80% cleared at 16 h (Fig. 4C). In a two way ANOVA, there was a significant interaction between construct (M1$_{R56H, P96H, Y102H}$-13A7-13A7-Nb80 vs. M1$_{R56H, P96H, Y102H}$-13A7-13A7) and time ($F_{1,20}$ = 4.5, p = 0.0094). Post-hoc comparisons were only significant for the 8 h time point (p = 0.027); the differences at earlier time points were not statistically significant after correction for multiple comparisons. Levels of an otherwise identical four nanobody construct including the M1$_{AA}$ mutation that does not bind TfR nor cross the BBB were undetectable (n = 3). Levels of a BBB crossing four nanobody construct in which 13A7 was replaced by Nb3, the anti-human amyloid-beta nanobody that does not bind any known targets in the wild-type mouse brain, peaked at approximately threefold lower levels than the P2X7 receptor binding construct (Fig. 4D). Two way ANOVA was again used to analyze the capillary depleted brain homogenate data. There were significant main effects of both construct (M1$_{R56H, P96H, Y102H}$-13A7-13A7-Nb80 vs. M1$_{R56H, P96H,}$
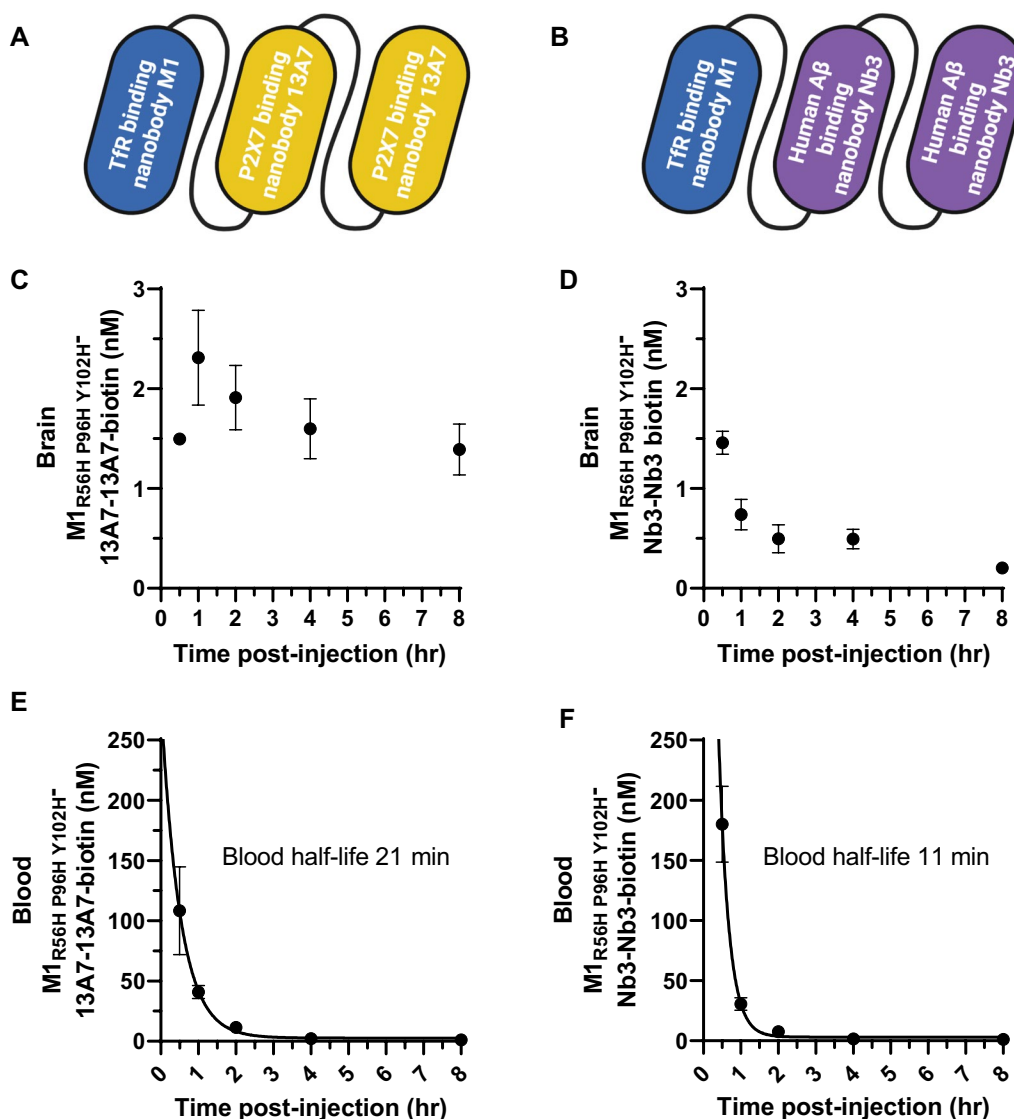
Fig. 3 BBB transcytosis of macromolecular cargos by M1$_{R56H, P96H, Y102H}$ and brain target engagement in vivo. **A** Diagram of the three nanobody construct including M1$_{R56H, P96H, Y102H}$ plus a tandem dimer of the P2X7 receptor binding nanobody 13A7 for brain target engagement. **B** Diagram of a control three nanobody construct including M1$_{R56H, P96H, Y102H}$ plus a tandem dimer of the human amyloid-beta binding nanobody Nb3 which has no known targets in the mouse brain. **C** Time course of capillary depleted lysate levels of biotinylated M1$_{R56H, P96H, Y102H}$-13A7-13A7 (n = 3 per time point) after iv injection of 30 nmol/kg. **D** Time course of capillary depleted lysate levels of biotinylated M1$_{R56H, P96H, Y102H}$-Nb3-Nb3 (n = 3 per time point) after iv injection of 30 nmol/kg. **E–F** Time course of blood levels of the biotinylated three nanobody constructs from the same mice as **C**, **D**

(See figure on next page.)

Fig. 4 Blood half-life extension using an albumin-binding nanobody further enhances in vivo BBB transcytosis of macromolecular cargos by M1$_{R56H, P96H, Y102H}$. **A** Diagram of four nanobody constructs including M1$_{R56H, P96H, Y102H}$, a tandem dimer of the P2X7 receptor binding nanobody 13A7 for brain target engagement or the human amyloid-beta binding nanobody Nb3 with no known mouse brain targets, plus the albumin binding nanobody Nb80. **B** Time course of blood levels of the biotinylated four nanobody constructs demonstrating extended 2.6 h half-life. **C** Time course of capillary depleted lysate levels of biotinylated M1$_{R56H, P96H, Y102H}$-13A7-13A7-Nb80 (n = 3 per time point) after iv injection of 30 nmol/kg. **D** Time course of capillary depleted lysate levels of biotinylated M1$_{R56H, P96H, Y102H}$-Nb3-Nb3-Nb80 (n = 3 per time point) after iv injection of 30 nmol/kg. **E**, **F** Size exclusion chromatography of a biotinylated M1$_{P96H}$-13A7-13A7-Nb80 prior to injection (**E**) and in brain homogenates (**F**) from 4 different mice (gray, red, orange, and blue symbols) 2 h after iv injection into wild-type mice at 300 nmol/kg body weight demonstrating integrity of the four nanobody constructs in brain. No substantial aggregation or degradation was apparent
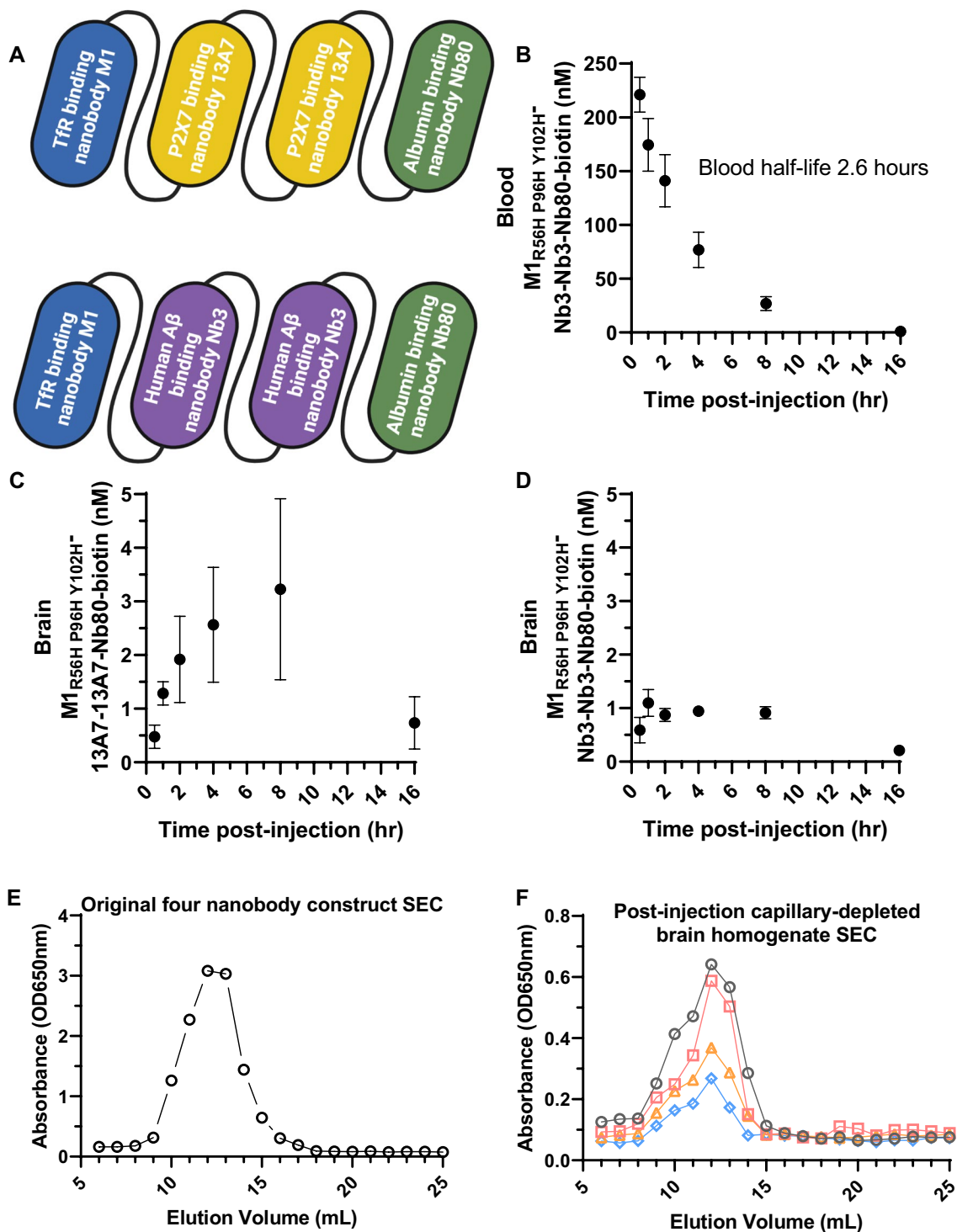
Fig. 4 (See legend on previous page.)

$_{Y102H}$-Nb3-Nb3-Nb80; $F_{1,24} = 18.2$, p = 0.0003) and time ($F_{5,24} = 5.8$, p = 0.0012), as well as a significant construct × time interaction ($F_{5,24} = 2.95$, p = 0.03). Post-hoc comparisons were significant for the 4 h (p = 0.034) and 8 h (p = 0.0014) time points. Biotinylated four nanobody construct levels in the capillary fractions were elevated at 30 min and 1 h, but below the limit of reliable quantitation (< 0.2 nM) at later times (Additional file 1: Fig. S4C-D).

Esparza *et al. Fluids and Barriers of the CNS*   (2023) 20:64

Page 11 of 17

Four nanobody constructs remained intact and were not detectibly degraded in the capillary depleted brain lysates; size exclusion chromatography revealed similar distribution of sizes in the capillary depleted lysates compared to the original injected material (Fig. 4E, F). These capillary depleted lysate results were compatible with the hypothesis that a modest prolongation of serum half-life of the $M1_{R56H, P96H, Y102H}$-based nanobody constructs produced higher peak brain levels of the biological macromolecule cargos and longer residence time in the brain.

Further confirmation of BBB crossing and brain target engagement was provided by in situ histochemistry using slices from the contralateral hemispheres of the same mice injected with four nanobody constructs described above. At 30 min after injection, the biotinylated four nanobody construct was detected in structures with morphologies consistent with capillaries (Fig. 5A and Additional file 1: Fig. S5A, B). At later times, cellular structures were labeled with increasing intensity (Fig. 5B–F and Additional file 1: Fig. S5C, D) in a pattern consistent with the ex vivo binding of the 13A7 nanobody construct (Fig. 5G). Peak binding appeared at 4–8 h, with reduced binding at 16 h. The time course of in situ binding was similar to that observed in the capillary depleted brain lysates. There was no detectible in situ histochemical signal 4 h after injection of the construct containing the $M1_{AA}$ mutation that does not bind TfR nor cross the BBB (Fig. 5H). There was faint staining in structures with morphologies consistent with capillaries but no detectible cellular structures on in situ histochemical signal after injection of the four nanobody construct in which 13A7 was replaced by Nb3 (Fig. 5I). Additional histochemical images showing consistent labeling in other brain regions are shown in Additional file 1: Figs. S6–7. Additional controls demonstrating minimal ex vivo binding of biotinylated $M1_{R56H, P96H, Y102H}$ and $M1_{R56H, P96H, Y102H}$-Nb3-Nb3-Nb80 are shown in Additional file 1: Fig. S8. These in situ histochemistry results provided further support for the hypothesis that $M1_{R56H, P96H, Y102H}$ was capable of shuttling proof-of-concept biological macromolecules across the BBB in vivo where they could specifically interact with brain targets.

Nonlinear relationship between administered dose and brain levels of shuttled macromolecular cargo

The utility of a BBB shuttle system for specific diagnostic and therapeutic applications may depend on the quantitative relationship between administered dose and achievable brain levels. We assessed the capillary depleted brain homogenate levels 4 h after injection of a wide range of doses of the biotinylated TfR and P2X7 receptor binding four nanobody construct (Fig. 6). As has been reported for another TfR-binding antibody fragment [45], a strong saturation effect was observed; peak capillary depleted brain homogenate levels were observed at 30 nmol/kg (approximately 1.8 mg/kg), with no increased levels after injections of much higher doses. At the lowest doses administered, 1 and 3 nmol/kg, the brain levels of 0.64 and 1.21 nM indicated that the construct was transported across the BBB at 13.4 and 8.8% of the injected dose/gram of brain tissue. At 30 nmol/kg, levels as high as 4.5 nM indicated that the construct was transported across the BBB at 3.5% injected dose/gram of brain tissue. Full calculations are shown in Additional file 1: Table S1. There were small *decreases* in capillary depleted brain homogenate levels after injection of higher doses. We performed mathematical curve fitting of two models to the dose response data. The first model involved fits to the standard Hill equation with 3 parameters, and the alternative model involved fits to a 3 parameter model that included substrate inhibition. The alternative model fit the data better ($r^2 = 0.75$ vs. 0.69). These results are compatible with the hypothesis that $M1_{R56H, P96H, Y102H}$ can shuttle proof-of-concept biological macromolecules across the BBB efficiently at low to moderate doses but becomes substantially less efficient at higher doses due to both saturation and an apparent substrate inhibitory effect.

Discussion

In summary, the mouse TfR-binding nanobody M1 with three histidine mutations can be used as a shuttle to transport other nanobodies across the intact BBB in mice. After intravenous injections of low to moderate doses, 1–30 nmol/kg, nanobody construct levels in capillary depleted brain lysates reached over 3.5% of injected dose per gram of brain, which is comparable to other top performing receptor mediated transcytosis shuttle systems (Additional file 1: Table S2). The kinetics of M1 nanobody-mediated BBB transcytosis were relatively fast. For a three nanobody construct, peak levels occurred at 1 h, and for a four nanobody albumin binding construct peak levers were noted at 4–8 h after injection with ~80% clearance from the brain by 16 h. The pH dependence of M1 histidine mutant binding partially correlated with in vivo BBB transport efficacy. This result is compatible with the hypothesis that unbinding of M1-based constructs in the relatively acidic environment of the intracellular vesicular compartments involved in transcytosis may favor fast delivery across the BBB (Fig. 7).

It is likely that there will not be a "one size fits all" best solution to the problem of transporting macromolecules across the BBB. Nanobody-based receptor mediated transcytosis shuttles such as the pH-dependent transferrin receptor binding system presented here may play an important context-specific role. Nanobodies can be
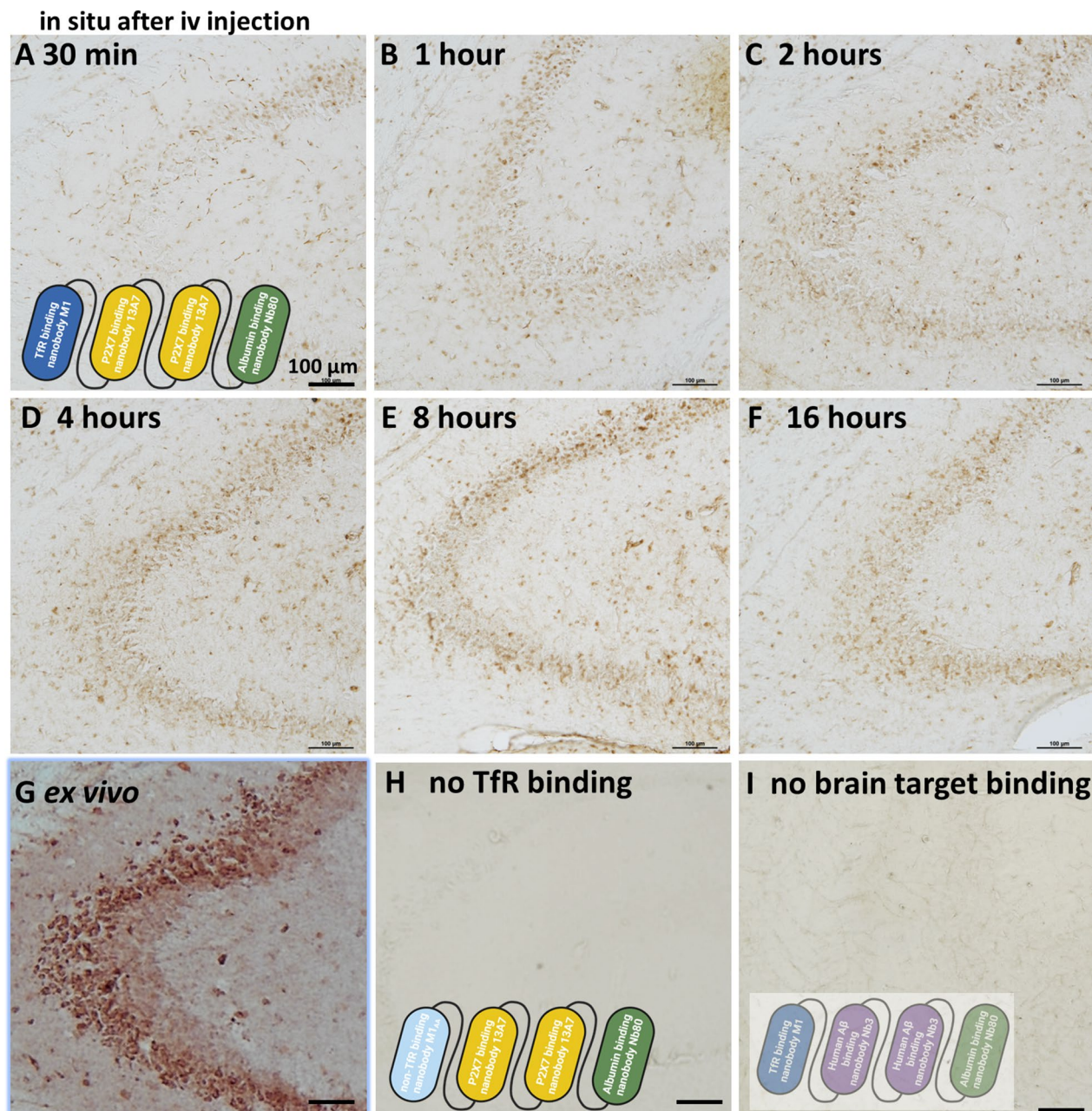
Fig. 5 In vivo target engagement of four nanobody constructs after iv injection. **A–F** In situ labeling of biotinylated M1$_{R56H, P96H, Y102H}$-13A7-13A7-Nb80 injected iv into wild-type mice at 600 nmol/kg body weight at 30 min showing largely labelling in structures with morphologies consistent with capillaries, and at 1, 2, 4, 8 and 16 h showing cellular labeling in hippocampus. **G** Positive control: ex vivo staining of naïve mouse brain slice with 50 nM biotinylated M1$_{R56H, P96H, Y102H}$-13A7-13A7-Nb80. **H** Negative control: no in situ labeling after intravenous injection of 600 nmol/kg M1$_{AA}$-13A7-13A7-Nb80 which does not bind mTfR. **I** Negative control: trace in situ labeling of structures with morphologies consistent with capillaries after intravenous injection of 600 nmol/kg M1$_{R56H, P96H, Y102H}$-Nb3-Nb3-Nb80. Nb3 has no known targets in wild-type mouse brain

readily engineered, inexpensively produced in bacterial and yeast systems, and stored at room temperature. Furthermore, the blood and brain kinetics were relatively fast, especially for the 3 nanobody constructs. Thus, applications requiring frequent re-engineering, low cost, simplified logistics, and rapid blood and brain kinetics may be favored. Examples could include development of a family of modular molecular imaging agents created by
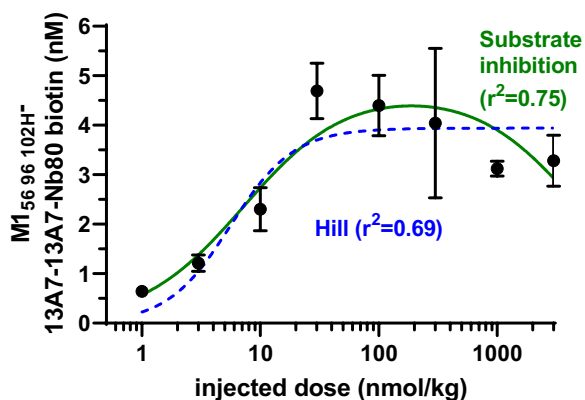
Fig. 6 Capillary depleted brain lysate levels of nanobody construct 4 h after injection of a range of doses of biotinylated M1$_{R56H, P96H, Y102H}$-13A7-13A70-Nb80 in mice. N = 3 per dose, except for N = 2 at 1 nmol/kg and N = 2 for 1000 nmol/kg. Hill equation fit parameters were B$_{max}$ = 3.94 nM, ED$_{50}$ = 5.6 nmol/kg, Hill coefficient = 1.6. Substrate inhibition fit parameters were B$_{max}$ = 4.7 nM, ED$_{50}$ = 7.3 nmol/kg, K$_i$ = 4877 nmol/kg

swapping out the P2X7 receptor binding nanobodies for other diagnostic marker-specific recognition domains. The relatively fast kinetics are potentially compatible with the workflow of diagnostic imaging involving injection of a contrast agent and scanning a few hours later. We have found that these nanobody constructs could be biotinylated via lysine conjugation without loss of efficacy, making it likely that conjugation of other labels such as metal chelators and fluorophores should also be feasible. A similar approach could be used to develop a family of relatively fast acting therapeutic agents, again by swapping out the P2X7 receptor binding nanobodies for other disease-specific therapeutic payloads. Of note, the first nanobody-based therapeutic approved for human use, caplacizumab for TTP, has rapid kinetics appropriate for acute treatment and once daily dosing [46].

The nanomolar levels of the M1 nanobody-based constructs detected in capillary depleted brain lysates after intravenous injection of readily achievable doses are
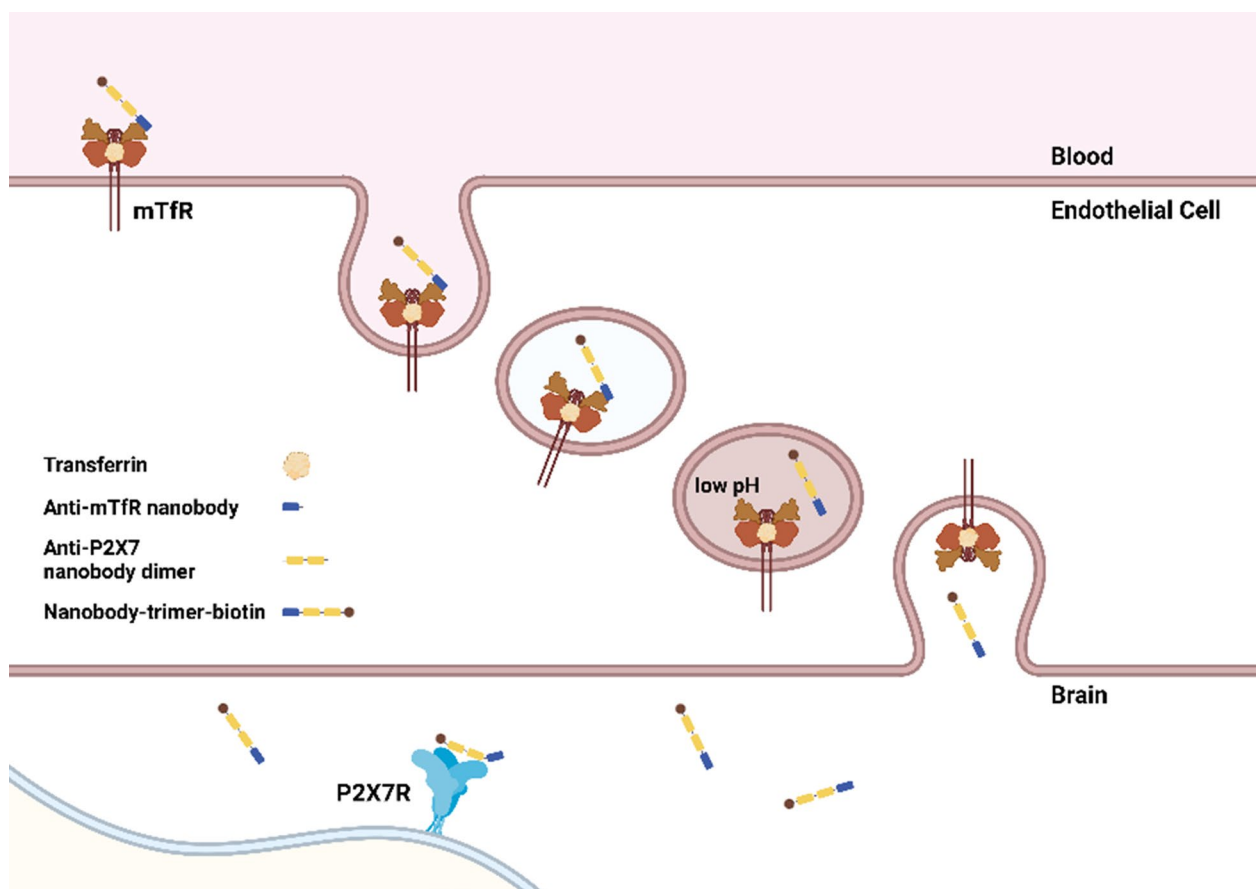
Fig. 7 Diagram of hypothesized mechanisms involved in BBB transcytosis of mTfR-and-P2X7-receptor binding nanobody constructs. Anti-mTfR nanobodies bind to mTfR in blood and constructs are endocytosed. Nanobody constructs unbind from mTfR in a pH-dependent fashion in intracellular vesicular compartments. Nanobody constructs are released into the brain and bind P2X7 receptor targets. (Produced using BioRender)

potentially compatible with many applications. PET scans using radioactive metal conjugates may be feasible given the high percent injected dose/gram of brain and high ratio of concentrations for active constructs vs. nontarget binding controls. Therapeutic applications should also be feasible for agents with relatively high affinity. It remains to be determined whether molecular contrast MRI using extremely small iron oxide nanoparticles [47] or other MRI contrast agents will be feasible. Fundamentally, the major limitation to applications requiring higher brain concentrations is the saturation of the transferrin receptor-based transport system. At injected doses above 30 nmol/kg no further increases in concentrations in capillary depleted brain lysates were observed. Saturation of the transferrin receptor-based transport system has been observed by others as well [45] (Additional file 1: Table S2), and to our knowledge transport of macromolecules via any receptor mediated transport system has not reached levels above ~ 13 nM in capillary depleted brain lysates [31]. The relationship between capillary depleted brain lysate concentrations and brain extracellular space concentrations has not been determined (see Supplemental Discussion).

The 13A7 P2X7 receptor binding nanobody was chosen primarily for demonstration of proof-of-concept, but BBB penetrating P2X7 receptor binding agents have many potential therapeutic applications. Brain P2X7 receptor activation has been implicated in the pathophysiology of traumatic brain injury, post-traumatic headache, ischemic and hemorrhagic stroke, multiple sclerosis, neurodegenerative disorders, depression, and other conditions [48–58]. Development of P2X7 receptor binding reagents has been an active area of pharmaceutical research, and there remains an unmet need for highly specific, brain-penetrating P2X7 receptor antagonists [59]. Administration of a P2X7 receptor binding nanobody intracerebroventricularly has been shown to reduce stroke lesions in a mouse model but P2X7 receptor binding nanobodies were not effective after intravenous administration [56], further emphasizing the importance of BBB penetration. However, the specificity of the 13A7 nanobody has not been fully established, and alternative nanobodies that bind to human P2X7 receptors may be more appropriate for human therapeutic use [42, 56, 60].

There are several limitations to these findings. First, our strategy for introducing histidine mutations to impart pH dependent binding was empirical rather than structure based. Despite intensive efforts, we and other have not yet been able to obtain high resolution structural information on the mouse TfR extracellular domain. If mouse TfR structures can be obtained, it would open the doors for further rational mutagenesis to impart even sharper pH dependent binding which in turn could further improve transcytosis. The structure of the human TfR extracellular domain has been solved [61, 62], so rational mutagenesis could be used to accelerate development of pH-dependent human TfR-binding nanobodies. Second, we have not yet been able to directly measure nanobody on and off rates at pH 5.5 and pH 7.4 for technical reasons (please see Supplemental Discussion); our measurements of pH-dependent apparent unbinding may not reflect true kinetics. Third, we have not performed detailed tracking of the transcytosis of the M1-based nanobody constructs. We do not know exactly where the presumed pH-dependent unbinding occurs from a cell biological perspective. It is also possible that the constructs do not unbind completely, but instead change their binding such that they are sorted differently though the transcytosis pathways. Full investigation of the relationships between affinity, pH dependent unbinding and BBB transcytosis are areas of ongoing effort. Likewise, we do not understand the mechanisms of clearance from the brain nor whether these clearance mechanisms are pH-dependent. Fourth, we have not performed a full quantitative assessment of the relationships between in vivo NT-induced hypothermia effects and in vivo concentrations in capillary depleted brain lysates for all of the tested constructs. We performed in vivo measurements in capillary depleted brain lysates only for our lead candidate, the $M1_{R56H, P96H, Y102H}$ mutant with the largest NT-induced hypothermia effect. NT-induced hypothermia likely reflects transcytosis across the BBB in the hypothalamus [63], and the hypothalamic BBB may not be identical to that of other parts of the brain, so the relationship between in vivo assays is not necessarily 1:1. Additional investigation of the relationships between affinity and pH dependent binding is ongoing. Fifth, while we have not observed overt toxicity after single dose injection of M1 nanobody constructs apart from one mouse that died shortly after injection, formal toxicity testing after single dose and multidose injection has not yet been performed. Sixth, we have not assessed the BBB transport capacity of the M1 nanobody mutants for other macromolecular cargoes such as full size antibodies, single chain variable fragments, enzymes, or nucleic acids. Relatedly, it is not clear whether brain cytosolic targets can be reached even when BBB crossing is efficient; both the NT receptor and P2X7 receptor are extracellular, as are most of the targets of macromolecular cargos assessed in previous work in the field (Additional file 1: Table S2). Seventh, the M1 nanobody mutants bind to mouse but not human TfR. Additional nanobodies binding to human TfR are in development and we plan to use the same histidine mutagenesis strategy to impart similar pH-dependent binding to human TfR binding nanobodies. There are other examples of human specific

Esparza *et al. Fluids and Barriers of the CNS*   (2023) 20:64

Page 15 of 17

TfR binding nanobodies that could also be engineered in this fashion [27]. Likewise, we have not yet 'humanized' our nanobody constructs, but the framework for doing so has been relatively well established [64]. It will be most appropriate to humanize nanobody constructs that bind to human targets. Finally, we have not yet used the M1 nanobody constructs for preclinical imaging or therapeutic studies. Imaging studies using the 3 nanobody constructs and fast-acting therapeutic studies using the 4 nanobody constructs are the logical next steps in this line of research given the rapid kinetics of these constructs and the important role of P2X7 receptors in many disease processes.

Conclusions

In conclusion, our results are compatible with the hypothesis that an engineered TfR-binding nanobody with pH-dependent unbinding has potential to serve as a shuttle system for transcytosis of biological macromolecules across the BBB and into the brain. Additional development will be required to determine whether this or other nanobody-based shuttle systems will be useful for diagnostic and therapeutic applications.

Abbreviations

BBB	Blood brain barrier
BSA	Bovine serum albumin
HABA	4′-Hydroxyazobenzene-2-carboxylic acid
HBSS	HEPES-buffered saline
IPTG	Isopropylthio-β-galactoside
iv	Intravenous
NT	Neurotensin
PBS	Phosphate-buffered saline
RIPA	Radioimmunoprecipitation assay
scFv	Single chain variable fragment
SDS PAGE	Sodium dodecyl sulfate polyacrylamide gel electrophoresis
SEC	Size exclusion chromatography
TfR	Transferrin receptor
WT	Wild-type

Supplementary Information

The online version contains supplementary material available at https://doi.org/10.1186/s12987-023-00462-z.

> **Additional file 1.** Supplemental information, including supplemental methods, supplemental results and figures, supplemental tables, supplemental discussion, and supplemental references.

Disclaimer

The views, information or content, and conclusions presented do not necessarily represent the official position or policy, nor should any official endorsement be inferred, on the part of the National Institutes of Health, the Uniformed Services University, the Department of Defense, Henry M. Jackson Foundation for the Advancement of Military Medicine, Inc., or other government agency.

Availability of data and materials

All protein and DNA sequences will be made available by request from the authors. Recombinant purified nanobody constructs and DNA vectors are available for sharing under appropriate material transfer agreements.

Declarations

Ethics approval and consent to participate

All animal experiments were conducted according to protocols approved by the NINDS intramural research program animal studies committee, protocol # 1406.

Consent for publication

Clearance has been obtained from the NINDS intramural research program and from the Uniformed Services University.

Competing interests

The authors declare that they have no conflicts of interest.

Author details

[1]National Institute of Neurological Disorders and Stroke, Bethesda, MD, USA. [2]Henry M. Jackson Foundation for the Advancement of Military Medicine, Inc, Bethesda, MD, USA. [3]Department of Biomedical Engineering, Washington University in St. Louis, St. Louis, MO, USA. [4]Center for Neuroscience and Regenerative Medicine, Bethesda, MD, USA. [5]Department of Neurology, Uniformed Services University of the Health Sciences, Bethesda, MD, USA.

References

1. Terstappen GC, Meyer AH, Bell RD, Zhang W. Strategies for delivering therapeutics across the blood-brain barrier. Nat Rev Drug Discov. 2021;20(5):362–83. https://doi.org/10.1038/s41573-021-00139-y.
2. Pardridge WM. A historical review of brain drug delivery. Pharmaceutics. 2022;14(6):1283. https://doi.org/10.3390/pharmaceutics14061283.
3. Friden PM, Walus LR, Musso GF, Taylor MA, Malfroy B, Starzyk RM. Anti-transferrin receptor antibody and antibody-drug conjugates cross the blood-brain barrier. Proc Natl Acad Sci USA. 1991;88(11):4771–5. https://doi.org/10.1073/pnas.88.11.4771.
4. Pardridge WM, Buciak JL, Friden PM. Selective transport of an anti-transferrin receptor antibody through the blood-brain barrier in vivo. J Pharmacol Exp Ther. 1991;259(1):66–70.
5. Khan AI, Liu J, Dutta P. Iron transport kinetics through blood-brain barrier endothelial cells. Biochim Biophys Acta Gen Subj. 2018;1862(5):1168–79. https://doi.org/10.1016/j.bbagen.2018.02.010.
6. Sonoda H, et al. A blood-brain-barrier-penetrating anti-human transferrin receptor antibody fusion protein for neuronopathic

mucopolysaccharidosis II. Mol Ther. 2018;26(5):1366–74. https://doi.org/10.1016/j.ymthe.2018.02.032.

7. Okuyama T, et al. A Phase 2/3 Trial of Pabinafusp Alfa, IDS fused with anti-human transferrin receptor antibody, targeting neurodegeneration in MPS-II. Mol Ther. 2021;29(2):671–9. https://doi.org/10.1016/j.ymthe.2020.09.039.

8. Boado RJ, Pardridge WM. Brain and organ uptake in the rhesus monkey in vivo of recombinant iduronidase compared to an insulin receptor antibody-iduronidase fusion protein. Mol Pharm. 2017;14(4):1271–7. https://doi.org/10.1021/acs.molpharmaceut.6b01166.

9. Giugliani R, et al. Neurocognitive and somatic stabilization in pediatric patients with severe Mucopolysaccharidosis Type I after 52 weeks of intravenous brain-penetrating insulin receptor antibody-iduronidase fusion protein (valanafusp alpha): an open label phase 1–2 trial. Orphanet J Rare Dis. 2018;13(1):110. https://doi.org/10.1186/s13023-018-0849-8.

10. Yogi A, et al. Brain delivery of IGF1R5, a single-domain antibody targeting insulin-like growth factor-1 receptor. Pharmaceutics. 2022;14(7):1452. https://doi.org/10.3390/pharmaceutics14071452.

11. Alata W, et al. Targeting insulin-like growth factor-1 receptor (IGF1R) for brain delivery of biologics. FASEB J. 2022;36(3):e22208. https://doi.org/10.1096/fj.202101644R.

12. Shin J-W, et al. Grabody B, an IGF1 receptor-based shuttle, mediates efficient delivery of biologics across the blood-brain barrier. Cell Rep Methods. 2022;2(11):100338. https://doi.org/10.1016/j.crmeth.2022.100338.

13. Zuchero YJY, et al. Discovery of novel blood-brain barrier targets to enhance brain uptake of therapeutic antibodies. Neuron. 2016;89(1):70–82. https://doi.org/10.1016/j.neuron.2015.11.024.

14. Edavettal S, et al. Enhanced delivery of antibodies across the blood-brain barrier via TEMs with inherent receptor-mediated phagocytosis. MED. 2022;3(12):860-882.e15. https://doi.org/10.1016/j.medj.2022.09.007.

15. Muruganandam A, Tanha J, Narang S, Stanimirovic D. Selection of phage-displayed llama single-domain antibodies that trans-migrate across human blood-brain barrier endothelium. FASEB J. 2002;16(2):240–2. https://doi.org/10.1096/fj.01-0343fje.

16. Georgieva JV, et al. Antibody screening using a human iPSC-based blood-brain barrier model identifies antibodies that accumulate in the CNS. FASEB J. 2020;34(9):12549–64. https://doi.org/10.1096/fj.202000851R.

17. Hamers-Casterman C, et al. Naturally occurring antibodies devoid of light chains. Nature. 1993;363(6428):446–8. https://doi.org/10.1038/363446a0.

18. Muyldermans S. Applications of nanobodies. Annu Rev Anim Biosci. 2021;9:401–21. https://doi.org/10.1146/annurev-animal-021419-083831.

19. Su S, Esparza TJ, Nguyen D, Mastrogiacomo S, Kim JH, Brody DL. Pharmacokinetics of single domain antibodies and conjugated nanoparticles using a hybrid near infrared method. Int J Mol Sci. 2021;22(16):8695. https://doi.org/10.3390/ijms22168695.

20. Ulrichts H, et al. Antithrombotic drug candidate ALX-0081 shows superior preclinical efficacy and safety compared with currently marketed antiplatelet drugs. Blood. 2011;118(3):757–65. https://doi.org/10.1182/blood-2010-11-317859.

21. Callewaert F, et al. Evaluation of efficacy and safety of the anti-VWF Nanobody ALX-0681 in a preclinical baboon model of acquired thrombotic thrombocytopenic purpura. Blood. 2012;120(17):3603–10. https://doi.org/10.1182/blood-2012-04-420943.

22. Scully M, et al. Caplacizumab treatment for acquired thrombotic thrombocytopenic purpura. N Engl J Med. 2019;380(4):335–46. https://doi.org/10.1056/NEJMoa1806311.

23. Scully M, et al. Long-term follow-up of patients treated with caplacizumab and safety and efficacy of repeat caplacizumab use: post-HERCULES study. J Thromb Haemost. 2022;20(12):2810–22. https://doi.org/10.1111/jth.15892.

24. Martin T, et al. Ciltacabtagene autoleucel, an anti-B-cell maturation antigen chimeric antigen receptor T-cell therapy, for relapsed/refractory multiple myeloma: CARTITUDE-1 2-year follow-up. J Clin Oncol. 2023;41(6):1265–74. https://doi.org/10.1200/JCO.22.00842.

25. Markham A. Envafolimab: first approval. Drugs. 2022;82(2):235–40. https://doi.org/10.1007/s40265-022-01671-w.

26. Keam SJ. Ozoralizumab: first approval. Drugs. 2023;83(1):87–92. https://doi.org/10.1007/s40265-022-01821-0.

27. Wouters Y, Jaspers T, Rué L, Serneels L, De Strooper B, Dewilde M. VHHs as tools for therapeutic protein delivery to the central nervous system. Fluids Barriers CNS. 2022;19(1):79. https://doi.org/10.1186/s12987-022-00374-4.

28. Wouters Y, Jaspers T, De Strooper B, Dewilde M. Identification and in vivo characterization of a brain-penetrating nanobody. Fluids Barriers CNS. 2020;17(1):62. https://doi.org/10.1186/s12987-020-00226-z.

29. Su S, Esparza TJ, Brody DL. Selection of single domain anti-transferrin receptor antibodies for blood-brain barrier transcytosis using a neurotensin based assay and histological assessment of target engagement in a mouse model of Alzheimer's related amyloid-beta pathology. PLoS ONE. 2022;17(10):e0276107. https://doi.org/10.1371/journal.pone.0276107.

30. Yu YJ, et al. Boosting brain uptake of a therapeutic antibody by reducing its affinity for a transcytosis target. Sci Transl Med. 2011;3(84):84ra44. https://doi.org/10.1126/scitranslmed.3002230.

31. Niewoehner J, et al. Increased brain penetration and potency of a therapeutic antibody using a monovalent molecular shuttle. Neuron. 2014;81(1):49–60. https://doi.org/10.1016/j.neuron.2013.10.061.

32. Kariolis MS, et al. Brain delivery of therapeutic proteins using an Fc fragment blood-brain barrier transport vehicle in mice and monkeys. Sci Transl Med. 2020. https://doi.org/10.1126/scitranslmed.aay1359.

33. Sade H, Baumgartner C, Hugenmatter A, Moessner E, Freskgård P-O, Niewoehner J. A human blood-brain barrier transcytosis assay reveals antibody transcytosis influenced by pH-dependent receptor binding. PLoS ONE. 2014;9(4):e96340. https://doi.org/10.1371/journal.pone.0096340.

34. Tillotson BJ, Goulatis LI, Parenti I, Duxbury E, Shusta EV. Engineering an anti-transferrin receptor ScFv for pH-sensitive binding leads to increased intracellular accumulation. PLoS ONE. 2015;10(12):e0145820. https://doi.org/10.1371/journal.pone.0145820.

35. Maeda K, Kato Y, Sugiyama Y. pH-dependent receptor/ligand dissociation as a determining factor for intracellular sorting of ligands for epidermal growth factor receptors in rat hepatocytes. J Control Release. 2002;82(1):71–82. https://doi.org/10.1016/s0168-3659(02)00126-8.

36. Klaus T, Deshmukh S. pH-responsive antibodies for therapeutic applications. J Biomed Sci. 2021;28(1):11. https://doi.org/10.1186/s12929-021-00709-7.

37. Schröter C, et al. A generic approach to engineer antibody pH-switches using combinatorial histidine scanning libraries and yeast display. MAbs. 2015;7(1):138–51. https://doi.org/10.4161/19420862.2014.985993.

38. Triguero D, Buciak J, Pardridge WM. Capillary depletion method for quantification of blood-brain barrier transport of circulating peptides and plasma proteins. J Neurochem. 1990;54(6):1882–8. https://doi.org/10.1111/j.1471-4159.1990.tb04886.x.

39. Stocki P, et al. Blood-brain barrier transport using a high affinity, brain-selective VNAR antibody targeting transferrin receptor 1. FASEB J. 2021;35(2):e21172. https://doi.org/10.1096/fj.202001787R.

40. Georgieva JV, Katt M, Ye Z, Umlauf BJ, Wenthur CJ, Shusta EV. The 46.1 antibody mediates neurotensin uptake into the CNS and the effects depend on the route of intravenous administration. Pharmaceutics. 2022;14(8):1706. https://doi.org/10.3390/pharmaceutics14081706.

41. Stocki P, et al. CDR3 Variants of the TXB2 Shuttle with Increased TfR1 Association Rate and Enhanced Brain Penetration. Pharmaceutics. 2023;15(3):739. https://doi.org/10.3390/pharmaceutics15030739.

42. Danquah W, et al. Nanobodies that block gating of the P2X7 ion channel ameliorate inflammation. Sci Transl Med. 2016;8(366):366162. https://doi.org/10.1126/scitranslmed.aaf8463.

43. Paraschiv G, Vincke C, Czaplewska P, Manea M, Muyldermans S, Przybylski M. Epitope structure and binding affinity of single chain llama anti-β-amyloid antibodies revealed by proteolytic excision affinity-mass spectrometry. J Mol Recognit. 2013;26(1):1–9. https://doi.org/10.1002/jmr.2210.

44. Shen Z, et al. A resource of high-quality and versatile nanobodies for drug delivery. iScience. 2021;24(9):103014. https://doi.org/10.1016/j.isci.2021.103014.

45. Sehlin D, Syvänen S, MINC faculty. Engineered antibodies: new possibilities for brain PET? Eur J Nucl Med Mol Imaging. 2019;46(13):2848–58. https://doi.org/10.1007/s00259-019-04426-0.

46. Sargentini-Maier ML, De Decker P, Tersteeg C, Canvin J, Callewaert F, De Winter H. Clinical pharmacology of caplacizumab for the treatment of patients with acquired thrombotic thrombocytopenic purpura. Expert

Esparza *et al. Fluids and Barriers of the CNS*   (2023) 20:64

Page 17 of 17

Rev Clin Pharmacol. 2019;12(6):537–45. https://doi.org/10.1080/17512 433.2019.1607293.

47. Kim JH, et al. Sensitive detection of extremely small iron oxide nanoparticles in living mice using MP2RAGE with advanced image co-registration. Sci Rep. 2021;11(1):106. https://doi.org/10.1038/s41598-020-80181-9.

48. Ryu JK, Jantaratnotai N, Serrano-Perez MC, McGeer PL, McLarnon JG. Block of purinergic P2X7R inhibits tumor growth in a C6 glioma brain tumor animal model. J Neuropathol Exp Neurol. 2011;70(1):13–22. https://doi.org/10.1097/NEN.0b013e318201d4d4.

49. Jassam YN, Izzy S, Whalen M, McGavern DB, El Khoury J. Neuroimmunology of traumatic brain injury: time for a paradigm shift. Neuron. 2017;95(6):1246–65. https://doi.org/10.1016/j.neuron.2017.07.010.

50. Zhao H, Chen Y, Feng H. P2X7 receptor-associated programmed cell death in the pathophysiology of hemorrhagic stroke. Curr Neuropharmacol. 2018;16(9):1282–95. https://doi.org/10.2174/1570159X166661805160 94500.

51. Ribeiro DE, Roncalho AL, Glaser T, Ulrich H, Wegener G, Joca S. P2X7 receptor signaling in stress and depression. Int J Mol Sci. 2019;20(11):2778. https://doi.org/10.3390/ijms20112778.

52. Francistiová L, et al. The role of P2X7 receptor in Alzheimer's disease. Front Mol Neurosci. 2020;13:94. https://doi.org/10.3389/fnmol.2020.00094.

53. Currò D, Navarra P, Samengo I, Martire M. P2X7 receptors exert a permissive effect on the activation of presynaptic AMPA receptors in rat trigeminal caudal nucleus glutamatergic nerve terminals. J Headache Pain. 2020;21(1):83. https://doi.org/10.1186/s10194-020-01153-y.

54. Di Lauro C, et al. P2X7 receptor blockade reduces tau induced toxicity, therapeutic implications in tauopathies. Prog Neurobiol. 2022;208:102173. https://doi.org/10.1016/j.pneurobio.2021.102173.

55. Ren W, Rubini P, Tang Y, Engel T, Illes P. Inherent P2X7 receptors regulate macrophage functions during inflammatory diseases. Int J Mol Sci. 2021;23(1):232. https://doi.org/10.3390/ijms23010232.

56. Wilmes M, et al. Blocking P2X7 by intracerebroventricular injection of P2X7-specific nanobodies reduces stroke lesions. J Neuroinflamm. 2022;19(1):256. https://doi.org/10.1186/s12974-022-02601-z.

57. Hu Y, Wang B, Li S, Yang S. Pyroptosis, and its role in central nervous system disease. J Mol Biol. 2022;434(4):167379. https://doi.org/10.1016/j.jmb.2021.167379.

58. Yin Y, et al. Leveraging the ATP-P2X7 receptor signalling axis to alleviate traumatic CNS damage and related complications. Med Res Rev. 2023. https://doi.org/10.1002/med.21952.

59. Lee S, Ha H, Jang J, Byun Y. Recent advances in the development of antidepressants targeting the purinergic P2X7 receptor. Curr Med Chem. 2023;30(2):164–77. https://doi.org/10.2174/09298673296662206291 41418.

60. Pinto-Espinoza C, et al. Effective targeting of microglial P2X7 following intracerebroventricular delivery of nanobodies and nanobody-encoding AAVs. Front Pharmacol. 2022;13:1029236. https://doi.org/10.3389/fphar.2022.1029236.

61. Lawrence CM, Ray S, Babyonyshev M, Galluser R, Borhani DW, Harrison SC. Crystal structure of the ectodomain of human transferrin receptor. Science. 1999;286(5440):779–82. https://doi.org/10.1126/science.286.5440.779.

62. Cheng Y, Zak O, Aisen P, Harrison SC, Walz T. Structure of the human transferrin receptor-transferrin complex. Cell. 2004;116(4):565–76. https://doi.org/10.1016/s0092-8674(04)00130-8.

63. Martin GE, Bacino CB, Papp NL. Hypothermia elicited by the intracerebral microinjection of neurotensin. Peptides. 1980;1(4):333–9. https://doi.org/10.1016/0196-9781(80)90011-x.

64. Vincke C, Loris R, Saerens D, Martinez-Rodriguez S, Muyldermans S, Conrath K. General strategy to humanize a camelid single-domain antibody and identification of a universal humanized nanobody scaffold. J Biol Chem. 2009;284(5):3273–84. https://doi.org/10.1074/jbc.M806889200.

Publisher's Note